PCCP

Accepted Manuscript

ROYAL SOCIETY OF CHEMISTRY

rsc.li/pccp

Reactive Collisions for NO($^2\Pi$)+N(^4S) at Temperatures Relevant to the Hypersonic Flight Regime

Otoniel Denis-Alpizar,[†] Raymond J. Bemish,[‡] and Markus Meuwly [*,¶]

Department of Chemistry, University of Basel, Klingelbergstrasse 80, CH-4056 Basel, Switzerland, Air Force Research Laboratory, Space Vehicles Directorate, Kirtland AFB, New Mexico 87117, USA, and Department of Chemistry, University of Basel, Klingelbergstrasse 80, CH-4056 Basel, Switzerland and Department of Chemistry, Brown University, Providence, Rhode Island, USA

E-mail: m.meuwly-at-unibas.ch

Abstract

The NO($X^2\Pi$)+N(^4S) reaction which occurs entirely in the triplet manifold of N_2O is investigated using quasiclassical trajectories and quantum simulations. Fully-dimensional potential energy surfaces for the ^{3}A′ and ^{3}A″ states are computed at the MRCI+Q level of theory and are represented using a reproducing kernel Hilbert space. The N-exchange and N_2-formation channels, are followed by using the multi-state adiabatic reactive molecular dynamics method. Up to 5000 K these reactions occur predominantly on the N_2O ^{3}A″ surface. However, for higher temperatures the

---

[*] To whom correspondence should be addressed

[†] Department of Chemistry, University of Basel, Klingelbergstrasse 80, CH-4056 Basel, Switzerland

[‡] Air Force Research Laboratory, Space Vehicles Directorate, Kirtland AFB, New Mexico 87117, USA

[¶] Department of Chemistry, University of Basel, Klingelbergstrasse 80, CH-4056 Basel, Switzerland and Department of Chemistry, Brown University, Providence, Rhode Island, USA

contributions of the $^3A'$ and $^3A''$ states are comparable and the final state distributions are far from thermal equilibrium. From the trajectory simulations a new set of thermal rate coefficients up to 20000 K are determined. Comparison of the quasiclassical trajectory and quantum simulations finds that a classical description is a good approximation as determined from the final state analysis.

1 Introduction

Nitric oxide (NO) plays a major role in the chemistry near the surface of vehicles during atmospheric re-entry in the hypersonic regime where it connects the dominate atomic N and O populations.[1] Therefore, reactions of nitric oxide with N and O must be considered. Modelling the thermochemistry in the re-entry flows requires the knowledge of rate coefficients for the bimolecular reactions involving these species at very high temperatures as well as the final state populations. At such extreme conditions quantitative experiments are difficult and expensive. Consequently, computational studies are vital for characterizing the reactivity or energy transfer in reactive or nonreactive encounters of such systems.

Recently, a study of NO formation in hypersonic boundary layers[1] around space vehicles during re-entry showed that the inclusion of the NO data in the models substantially modified the mass fraction and the heat flux in the boundary layers. The reactions of NO with N proceed through N_2O. The singlet ($^1\Sigma^+$) ground state of N_2O has been studied intensely using both, theory[2–4] and experiment.[5–10] Conversely, the potential energy surfaces (PESs) that connect the ground states of the reactant ($NO(X^2\Pi)$+$N(^4S)$) and product ($N_2(X^1\Sigma)$+$O(^3P)$) side correlate with N_2O in its triplet states, see Figure 1. On the product side, the spin-inverting process $O(^1D)+N_2 \rightarrow O(^3P)+N_2$ has also been investigated using computation[11] and experiment.[12] For temperatures between 200 K and 300 K the rate coefficients are slowly varying and around 4×10^{-11} cm^3 molecule^{-1}s^{-1}.[12] Several experimental studies of the $NO(X^2\Pi)+N(^4S)\rightarrow N_2(X^1\Sigma)+O(^3P)$ reaction have been performed over the past decades[10,13–19] but the agreement between these experiments is poor. As an example, at 100 K Fox[15] derived a rate of 3.60×10^{-13} $\mathrm{cm^3 molecule^{-1} s^{-1}}$ from atmospheric models and data from the Viking 1 mission while Bergeat *et al*[13] obtain a value of 4.11×10^{-11} $\mathrm{cm^3 molecule^{-1} s^{-1}}$ using a resonance fluorescence technique.

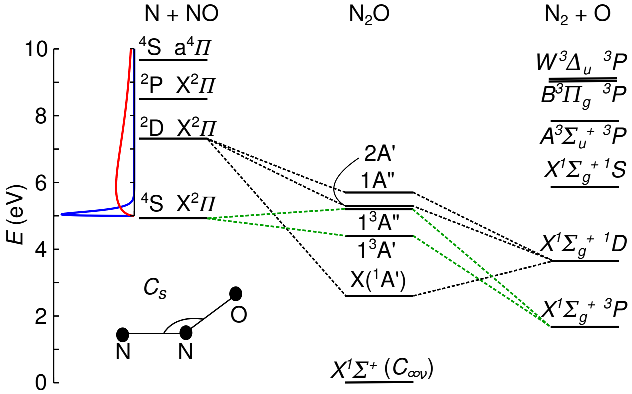

Figure 1: Schematic representation of the C_s (∢NON near 130°) partial adiabatic correlation diagrams for N_2O. Data taken from Ref.[20] The zero of energy is the energy of the linear $X^1\Sigma^+$ state of N_2O. The green lines correspond to the electronic states of interest for this work. A Maxwell-Boltzmann distribution at 1000 K (blue) and 20000 K (red) are also included to indicate initial populations at theses temperatures.

Theoretical studies of the scattering on the adiabatic electronic states have been carried out on the $^3A'$ and $^3A''$ surfaces.[21–25] An earlier PES, which has been considered to be the most accurate one until recently,[1] was based on a many-body expansion derived from a grid of *ab initio* energies computed at the CASPT2 level using a cc-pVTZ basis set.[23] Very recently, new PESs for the two lowest triplet states were determined at the multi reference configuration interaction (MRCI+Q) level of theory using the maug-cc-pVTZ basis set[26] and showed remarkable differences with the earlier PES. For example, the global minimum of the $^3A''$ state was found to be 0.23 eV deeper than in the previous work. For the $^3A'$ state several new minima and transition states were found. Therefore, PESs at the MRCI level are required for computing meaningful rates from dynamics calculations. The most recent PESs were then used to study the $N_2 + O \longrightarrow NO + N$ forward reaction based on QCT simulations. However, the reverse $NO + N \longrightarrow N_2 + O$ reaction was not considered because these surfaces do not have the correct long-range radial dependence which is essential.[25,26]

In the present work the PESs for the ^{3}A$'$ and ^{3}A$''$ states of N_2O are determined at the MRCI+Q/cc-pVTZ level of theory and represented as a reproducing kernel Hilbert space (RKHS). Such a treatment reproduces the points from electronic structure calculations exactly and captures the correct R^{-6} decay for dipole-induced dipole interactions. These PESs are subsequently used to study all possible channels of the NO($X^2\Pi$)+N(^4S) reaction using reactive surfaces based on the multi state adiabatic reactive MD (MS-ARMD) method.[27] Both, quasiclassical trajectory and quantum calculations are carried out for validating the use of classical mechanics for this problem. Finally, thermal rate coefficients for the high temperatures (5000 K to 20000 K) relevant at the hypersonic flight regime for N_2 formation and nitrogen exchange channels are computed and fit to simple empirical expressions. The remainder of this work is organized as follows. In the next section, the methods used for developing the PESs are described, and the quasiclassical trajectory simulations and their analysis are summarized. The results are discussed in Section 3, and conclusions are given in Section 4.

2 Methods

Ab Initio calculations

The *ab initio* potential energies of the triplet states of N_2O were computed at the multireference configuration interaction (MRCI) level including the Davidson correction (MRCI+Q),[28] preceded by complete active space self-consistent field (CASSCF) calculations. Dunning's correlation consistent polarized triplet-zeta (cc-pVTZ) basis set[29] was used. All electronic structure calculations were performed with the Molpro package.[30]

For both electronic states, ^{3}A$'$ and ^{3}A$''$, the asymptotic N_2+O and NO+N channels were treated separately. In each case, a three-dimensional grid of energies for the respective Jacobi coordinates (R, r, θ) was computed. For N_2+O, the angles vary between 0 and 90°. The angular interval was extended up to 180°, taking into account the symmetry of the system. In this way, the number of angular points is the same as for NO+N, which is necessary for the RKHS representation (see below). In total, 11 angular cuts were taken into account for each channel. MRCI+Q calculations for the ^{3}A$'$ state of the N_2+O asymptote were carried out for 19 distances along R ($R \in [1.1, 10.0]$ Å), and 13 points along r ($r \in [0.90, 1.47]$ Å) whereas for the NO+N asymptote they included $R \in [1.0, 10.0]$ Å and $r \in [0.90, 1.55]$ Å. For the ^{3}A$''$ state the same R intervals were used whereas for the N_2+O channel $r \in [0.90, 1.55]$ Å and $r \in [0.90, 1.58]$ Å for the NO+N channel. These grids for the diatomic distances r cover vibrational quantum numbers $v \leq 15$ and should be appropriate for the present work. However, more highly excited vibrational states may be represented less accurately.

Representation of the PESs

All PESs were represented by using a reproducing kernel Hilbert space approach.[31] The potential energy for each channel is

$$V(\mathbf{x}) = \sum_{\mathrm{k}=1}^{M} \alpha_{\mathrm{k}} Q(\mathbf{x}_{\mathrm{k}}, \mathbf{x}) \qquad (1)$$

where M is the number of *ab initio* points, $\mathbf{x}$ is the vector of internal coordinates $\mathbf{x} = (R, r, z)$, with $z = \frac{(1-\cos\theta)}{2}$, and $\mathbf{x}_{\mathrm{k}}$ corresponds to a grid point $\mathbf{x}_{\mathrm{k}} = (R_{\mathrm{k}}, r_{\mathrm{k}}, z_{\mathrm{k}})$. $Q(\mathbf{x}_{\mathrm{k}}, \mathbf{x})$ is the reproducing kernel for a multidimensional PES, which is obtained by the multiplication of three 1-dimensional reproducing kernels $q(x_{\mathrm{k}}, x)$

$$Q(\mathbf{x}_{\mathrm{k}}, \mathbf{x}) = q^{2,6}(R_{\mathrm{k}}, R) q^{2,6}(r_{\mathrm{k}}, r) q^{2}(z_{\mathrm{k}}, z) \qquad (2)$$

where $q^{2,6}(R_k, R)$ and $q^2(z_k, z)$ are the radial and angular kernels,[31]

$$q^{2,6}(R_k, R) = \frac{1}{14} R_>^{-7} \left\{ 1 - \frac{7R_<}{9R_>} \right\} \tag{3}$$

$$q^2(z_k, z) = 1 + z_< z_> + 2z_<^2 z_> \left\{ 1 - \frac{z_<}{3z_>} \right\} \tag{4}$$

The subscripts $R_>$ and $R_<$ are, respectively, the greater and smaller of any pair of number R_k and R and similar for $z_>$ and $z_<$. The coefficients α_k are determined from solving the linear system

$$\begin{pmatrix} Q(\mathbf{x}_1, \mathbf{x}_1) & Q(\mathbf{x}_1, \mathbf{x}_2) & \cdots & Q(\mathbf{x}_1, \mathbf{x}_\mathrm{M}) \\ Q(\mathbf{x}_2, \mathbf{x}_1) & Q(\mathbf{x}_2, \mathbf{x}_2) & \cdots & Q(\mathbf{x}_2, \mathbf{x}_\mathrm{M}) \\ \vdots & \vdots & \ddots & \vdots \\ Q(\mathbf{x}_\mathrm{M}, \mathbf{x}_1) & Q(\mathbf{x}_\mathrm{M}, \mathbf{x}_2) & \cdots & Q(\mathbf{x}_\mathrm{M}, \mathbf{x}_\mathrm{M}) \end{pmatrix} \begin{pmatrix} \alpha_1 \\ \alpha_2 \\ \vdots \\ \alpha_\mathrm{M} \end{pmatrix} = \begin{pmatrix} V(\mathbf{x}_1) \\ V(\mathbf{x}_2) \\ \vdots \\ V(\mathbf{x}_\mathrm{M}) \end{pmatrix} \tag{5}$$

By construction, reproducing kernels decay to zero for $R \to \infty$. Hence, for a correct representation of the asymptotic behaviour of the kernel interpolation, the energy at large atom-diatom distance $V(R \to \infty, r, \theta)$ was subtracted from the values of the grid, such that each cut $V^\mathrm{cut}(R, r, \theta)$ dissociates to zero. The potential $V^\mathrm{cut}(R, r, \theta)$ is then represented as an RKHS following Equation 1. The asymptotic energies $V(R \to \infty, r, \theta)$, which are isotropic to a very good approximation, are also fitted using a 1-dimensional kernel. Then, the total energy is recovered by summing the energies of both interpolations $V(R, r, \theta) = V^\mathrm{cut}(R, r, \theta) + V(R \to \infty, r, \theta)$. The procedure is similar to that used for Ar+N_2^+.[32]

The reactive PES was constructed by smoothly connecting the three PESs (N^aO+N^b, N^bO+N^a, and N_2+O, where superscripts a and b are used to identify the N atoms), each represented as a RKHS (Eq. 1) with a distance-dependent switching function, as was previously done for NO_2.[33,34] The global PES is therefore

$$V(\mathbf{y}) = \sum_{i=1}^{3} w_i(\mathbf{y}) V_i(\mathbf{y}) \tag{6}$$

where $\mathbf{y} = (y_1, y_2, y_3)$ is the vector of the three inter-atomic distances of the N_2O molecule, and V_i are the potential energies of the three asymptotic PESs. The switching function is

$$w_i(\mathbf{y}) = \frac{e^{-(y_i/a)^4}}{\sum_{j=1}^{3} e^{-(y_j/a)^4}} \tag{7}$$

where y_i is any of the three inter-atomic distances. The term in the denominator is the normalization and the parameter a is 1.0 for the ^{3}A$'$ PES and 1.2 for the ^{3}A$''$ surface. This parameter determines the range over which the PESs are mixed.[27]

In the asymptotic reactant or product channels, the full weight is on the corresponding RKHS PES. On the other hand, in the well region where the grid is sufficiently dense, the RKHS representation determines the shape because it exactly reproduces the *ab initio* reference energies. However, if two atom-atom distances are comparable and small and two PESs have non-negligible weights $w_i(\mathbf{y})$, the global PES in Eq. 6 may exhibit small oscillations. For that reason, the radial extent of each grid was chosen sufficiently large for having meaningful weight at the geometries of the stationary points previously reported in the literature. The Fortran codes of both reactive PESs (^{3}A$'$ and ^{3}A$''$) are available from the authors or on GitHub.[35]

Furthermore, an independent grid of points at the MRCI+Q level of theory was computed for the diatomic molecules N_2 and NO. These points were fitted to a Morse potential function using a least squares procedure. Table 1 summarizes the properties of both molecules. The dissociation energy is lower than the experimentally measured one. However, this should not affect the calculations as full dissociation of N_2O into N+N+O is not considered here. These Morse parameters are then used for generating initial conditions for the quasiclassical trajectory (QCT) studies. The reason for preferring a computed potential energy curve for the diatomics over curves derived from experiments is to work with and validate an approach based entirely on computations.

Table 1: Morse parameters and observables computed from them, compared with experimental data for N_2 and NO.

	r_e (Å)	D_e (eV)	β (Å^{-1})	ω_e (cm^{-1})	$\omega_e x_e$ (cm^{-1})
N_2					
calc.	1.105	9.385	2.799	2389.579	18.858
expt.	1.098	9.905		2358.570	14.324
NO					
calc.	1.158	6.234	2.942	1982.032	19.532
expt.	1.151	6.614		1904.200	14.075

Experimental values from Ref.[36]

QCT calculations

Quasiclassical trajectory calculations are used to determine thermal rates coefficients from

$$k(T_t, T_v, T_r, T_e) = \sqrt{\frac{8\beta_t^3}{\pi\mu}} \int_0^\infty \sigma(E_c; T_t; T_v) E_c e^{-\beta_t E_c} dE_c \tag{8}$$

where T_t, T_v, T_r and T_e are the translational, vibrational, rotational and electronic temperatures, $\beta_i = 1/(k_B T_i)$, i denotes the respective temperature, k_B is the Boltzmann constant and E_c is the collisional energy. Initially, the various degrees of freedom in the reactants are assumed to be in thermal equilibrium, i.e. $T_\mathrm{t} = T_\mathrm{v} = T_\mathrm{r} = T_\mathrm{e} \equiv T$ for the remainder of the work. The cross section $\sigma(E_\mathrm{c};T)$ (using $T = T_\mathrm{v} = T_\mathrm{r} = T_\mathrm{e}$) is defined as

$$\sigma(E_\mathrm{c};T) = \sum_{\nu=0}^{\nu_\mathrm{max}} \sum_{j=0}^{j_\mathrm{max}(\nu)} \frac{(2j+1)e^{-\beta E_{\nu j}}}{Q_\mathrm{rv}} \sigma(E_\mathrm{c};\nu,j) \tag{9}$$

where Q_rv is the rovibrational partition function, ν and j are the vibrational and rotational quantum numbers, $E_{\nu j}$ is the respective internal energy in the state (ν,j), and ν_max and j_max are the maximum values of ν and j allowed by the available energy. The state-to-state cross section is

$$\sigma(E_\mathrm{c};\nu,j) = 2\pi \int_0^\infty P_{\nu j}(b;E_\mathrm{c}) b db \tag{10}$$

where $P_{\nu j}(b;E_\mathrm{c})$ is the opacity function, and b the impact parameter.

The dynamics of the system is followed by propagating the equations of motions for a given set of initial conditions. These equations were integrated numerically using the Velocity-Verlet algorithm.[37] The initial conditions for NO were generated from a WKB-quantized periodic orbit[38] of the corresponding rotating Morse oscillator for a given ν and j.[39] The symmetry axis of NO, the axis of its rotation, and the angular momentum were randomly oriented and the integral Eq. 8 was evaluated using an Importance Sampling Monte Carlo scheme.[40] The rotational and vibrational quantum numbers and the collision energy E_c were sampled using the probability distributions

$$p_{\nu j}(T) = \frac{(2j+1)e^{(-\beta E_{\nu j})}}{\sum\limits_{\nu'=0}^{\nu_\mathrm{max}} \sum\limits_{j'=0}^{j_\mathrm{max}(\nu')} (2j'+1)e^{-\beta E_{\nu' j'}}} \tag{11}$$

and

$$\rho(E_c)dE_c = \beta^2 E_c e^{-\beta E_c} dE_c \tag{12}$$

The impact parameter was sampled from 0 to b_max using an Importance Sampling Monte

Carlo scheme from which the rate coefficient is determined as

$$k(T) = g_{\mathrm{e}}(T)\sqrt{\frac{8}{\mu\pi\beta}}\frac{2\pi b_{\mathrm{max}}}{N_{\mathrm{tot}}}\sum_{k=1}^{N_{\mathrm{reac}}} b_{\mathrm{k}} \tag{13}$$

where N_{tot} and N_{reac} are the total and the reactive number of trajectories, respectively, and b_{k} is the impact parameter of reactive trajectory k. This last equation includes the electronic degeneracy factor $g_{\mathrm{e}}(T)$, which is

$$g_{\mathrm{e}}(T) = q_{\mathrm{N_2O}}(T)q^{-1}_{\mathrm{N(^4S)}}(T)q^{-1}_{\mathrm{NO(^2\Pi)}}(T) \tag{14}$$

where the electronic partition functions are $q_{\mathrm{N_2O}} = 3$ (for both states $1^3\mathrm{A}'$ and $1^3\mathrm{A}''$), $q_{\mathrm{N(^4S)}} = 4$ and $q_{\mathrm{NO(^2\Pi)}}(T) = 2 + 2\exp(-177.1/T)$. The $q_{\mathrm{NO(^2\Pi)}}(T)$ term takes into account the two spin-orbit states for $\mathrm{NO(^2\Pi)}$ and is $q_{\mathrm{NO(^2\Pi)}}(T) = g(^2\Pi_{3/2}) + g(^2\Pi_{1/2})\exp(-\Delta/RT)$, $g(^2\Pi_{1/2}) = g(^2\Pi_{3/2}) = 2$, and $\Delta = 177.1$ K is the spin-orbit splitting between the two states.[3] The $g_{\mathrm{e}}(T)$ term varies from 3/8 at low T to 3/16 at high T with most of the variation for temperatures below 300 K.

Overall, 10000 trajectories at nine temperatures between 100 K and 20000 K were computed. For each temperature, conservation of the total energy was verified. A time step of 0.01 fs was used, and the maximum impact parameter was set large enough that only non-reactive collisions take place ($b_{\mathrm{max}} = 10.05$ A and 9.58 A for the $^3\mathrm{A}'$ and $^3\mathrm{A}''$ respectively). The initial atom-diatom separation was the maximum value of 15 $\mathrm{a_0}$ (7.94 Å) or the impact parameter $b + 5$ $\mathrm{a_0}$ ($b + 2.65$ Å). For several T, a second set of calculations was run with a small value of b_{max} in order to increase the number of trajectories in the nitrogen exchange channel $\mathrm{N}^a\mathrm{O}+\mathrm{N}^b \longrightarrow \mathrm{N}^b\mathrm{O}+\mathrm{N}^a$. The total rate coefficients were summed from the rate coefficients on each PES,

$$k(T) = k_{\mathrm{p}}(T) + k_{\mathrm{pp}}(T) \tag{15}$$

where k_p and k_pp are the rate coefficients from simulations on the $^3\mathrm{A}'$ and $^3\mathrm{A}''$ PES, respectively.

3 Results

Quality of the Potential Energy Surfaces

The quality of the RKHS PESs (lines) compared to the *ab-initio* calculations (symbols) is illustrated in Figure 2. The cusps are due to crossing with higher excited electronic states which are well captured by the RKHS representations but were one of the main causes of errors in earlier PESs.[26] The behaviour of the energy as a function of R at the angles represented in this figure for a typical cut at $r_\mathrm{NO} = 1.3$ Å, shows the pronounced angular dependence of the PESs.

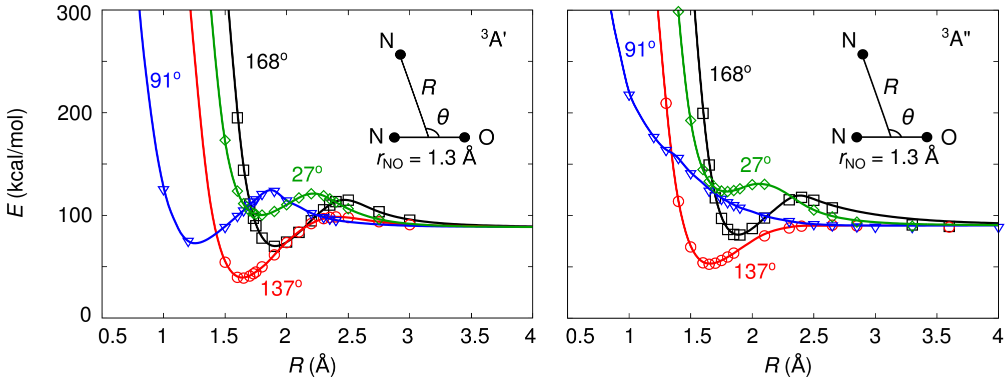

Figure 2: One-dimensional potential energy curves for the NO+N grid at $r_\mathrm{NO} = 1.3$ Å for several values of θ and the $^3\mathrm{A}'$ (left) and $^3\mathrm{A}''$ (right) states. The symbols are the *ab initio* energies and the solid lines are the global PESs. The zero of energy corresponds to the minimum of the $\mathrm{N}_2(^1\Sigma)$+$\mathrm{O}(^3P)$ asymptotic PES.

The experimental relative energies of the different channels can be compared with the analytical PESs, see Table 2. The present PESs underestimate the experimentally determined reaction energy ($\mathrm{NO+N}\rightarrow\mathrm{N_2+O}$) by less than 4% while for full atomization this value reduces to 1.5%. This is in contrast to the most recent PES which used an empirical extrapolation

Table 2: Reaction energies from the present calculations on the ^{3}A$''$ and ^{3}A$'$ PESs compared with the corresponding experimental data and with previous theoretical data (in kcal/mol).

Reaction	This work		Ref[26]		Exp[41]
	^{3}A$'$	^{3}A$''$	^{3}A$'$	^{3}A$''$	
NO($^2\Pi$)+N(^4S)$\rightarrow$N(^4S)+N(^4S)+O(^3P)	154.89	154.92	153.00	153.00	152.60
N_2($^1\Sigma$)+O(^3P)$\rightarrow$N(^4S)+N(^4S)+O(^3P)	228.02	228.01	227.80	228.00	228.40
N_2($^1\Sigma$)+O(^3P)$\rightarrow$NO($^2\Pi$)+N(^4S)	73.12	73.09	74.80	75.00	75.80

procedure for matching the energies of the reactant and products to the experimental ones which is probably not valid unconditionally for the entire surface.[26] Here it was decided to avoid such an empirical approach as the long-term goal is geared towards probing the performance of such computations at a given level of theory which can eventually be improved by morphing.[42] Furthermore, it is not expected that these differences lead to quantitatively different results.

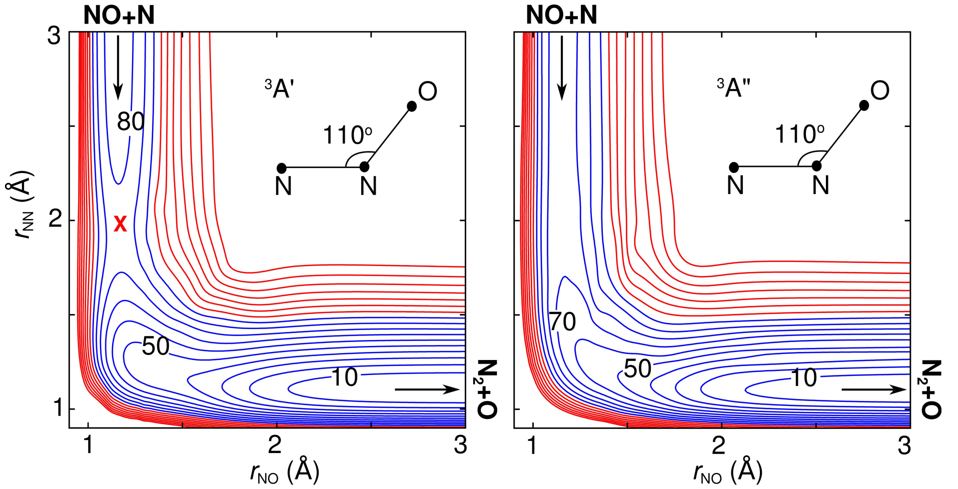

Figure 3: Contour plots at the NNO angle of 110°. Contours are shown in increments of 10 kcal/mol (blue contours for $E \leq 100$ kcal/mol and red contours for $E > 100$ kcal/mol). The X shows the barrier in the entrance channel of the ^{3}A$'$ PES. The zero of energy corresponds to the minimum of the N_2($^1\Sigma$)+O(^3P) asymptotic PES.

The NO+N $\longrightarrow$ N_2+O reaction is barrierless only on the ^{3}A$''$ surface as can be seen in Figure 3. On the ^{3}A$'$ PES the NO+N entrance channel exhibits a barrier of $\sim$ 11 kcal/mol which influences the reaction kinetics particularly at low temperatures. Also, it is worth noting that the nitrogen exchange reaction (N^aO+N^b $\rightarrow$$N^bO$+$N^a$) has a barrier in both states. Contour-plots for the $^3A''$ and $^3A'$ states highlighting the angular dependence are shown in Figure 4. The $^3A'$ surface has a larger number of stationary points (see Figure 4B) than the $^3A''$ (see Figure 4A). For the $^3A'$ state almost all the stationary points have one N–O distance close to 1.3 Å, see Figure 4B. A similar topography was found in Figure 9 of Ref.[26] This agreement was expected as the *ab initio* calculations in both studies were carried out at the MRCI level, even though in the present study the energies were computed using the slightly smaller cc-pVTZ basis set. Here, the energies are represented with a reproducing kernel while Lin *et al* employed a fitting function consisting of a sum of pairwise terms and permutationally invariant polynomials in bond orders. The main difference is that the PESs of the present work can be employed to study both, NO+N collisions (including atom exchange) and N_2 formation for the N_2+O channel. The long range part of the potential is described by the $q^{2,6}(R_\mathrm{k}, R)$ kernel which gives the correct long range behaviour (R^{-6}).

Dynamics

Quasiclassical Dynamics: The PESs were used to follow the different reaction channels for temperatures ranging from 100 K to 20000 K. Figure 5 shows the final state probability distributions of the rovibrational energy, and the vibrational and rotational quantum numbers at 5000 K for both products, NO and N_2, separately. Panels *a* and *d* show the probability distribution as a function of the final rovibrational energy of NO and N_2. It can be seen that formation of N_2 with low rovibrational energies occurs on the $^3A''$ state but not for $^3A'$ at 5000 K. The $^3A''$ surface allows direct reactions (no barrier), is more anisotropic at short range than the $^3A'$ PES which favours exchange of energy between different degrees of freedom and leads to N_2 in the ground vibrational state. The atom exchange reaction (N^aO+N^b $\longrightarrow$ N^bO+N^a) on both ($^3A'$ and $^3A''$) surfaces is improbable and occurs only for 0.3 % and 0.7 % of the trajectories at 5000 K, respectively. Therefore, exchange contribution

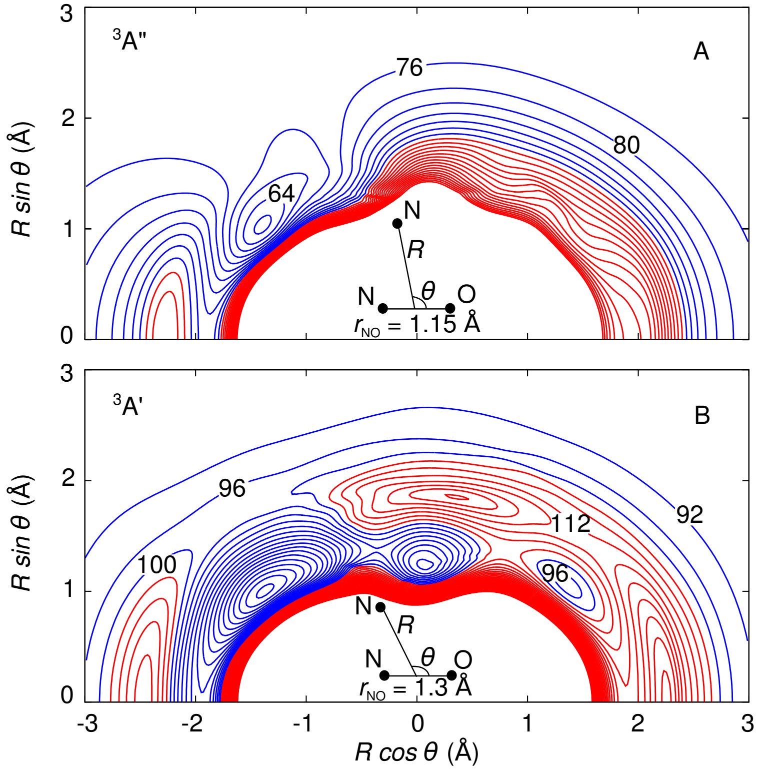

Figure 4: Potential energy surface for NO+N at $r_{\rm NO} = 1.15$ Å for the ^{3}A$''$ state (A) and the ^{3}A$'$ state with $r_{\rm NO}$ fixed at 1.3 Å (B). In the ^{3}A$'$ surface, at the represented NO-separation almost all stationary points can be seen. Contours are in increments of 4 kcal/mol (blue lines are used for $E \leq 100$ kcal/mol and red line for $E > 100$ kcal/mol). The zero of energy corresponds to the valley of the N_2+O asymptotic PES.

to the final distributions of NO is negligible and the scattering $\rm N^aO+N^b \longrightarrow N^aO+N^b$ is the predominant process on both surfaces. In this case, $\Delta\nu = 0$ are the most favoured transitions with a probability of 89% in the ^{3}A$'$ state and 82% on the ^{3}A$''$ surface. The averaged final vibrational energies $\langle E_\nu \rangle = \sum_{\rm i} p(\nu_{\rm i}) E^i_\nu$ of the products (NO and N_2) provide further support for the differences between the dynamics on the two electronic states. The difference in $\langle E_\nu \rangle$ shows clearly that N_2 produced from reactions on the ^{3}A$'$ PES is vibrationally hot compared to that from reactions taking place on the ^{3}A$''$ PES. The rotational distribution of N_2 in both electronic states do not show a clear Boltzmann distribution. However the number of trajectories that leads to N_2 is not large enough for a firm conclusion.

Figure 6 reports the probability distributions of the rovibrational energies together with the

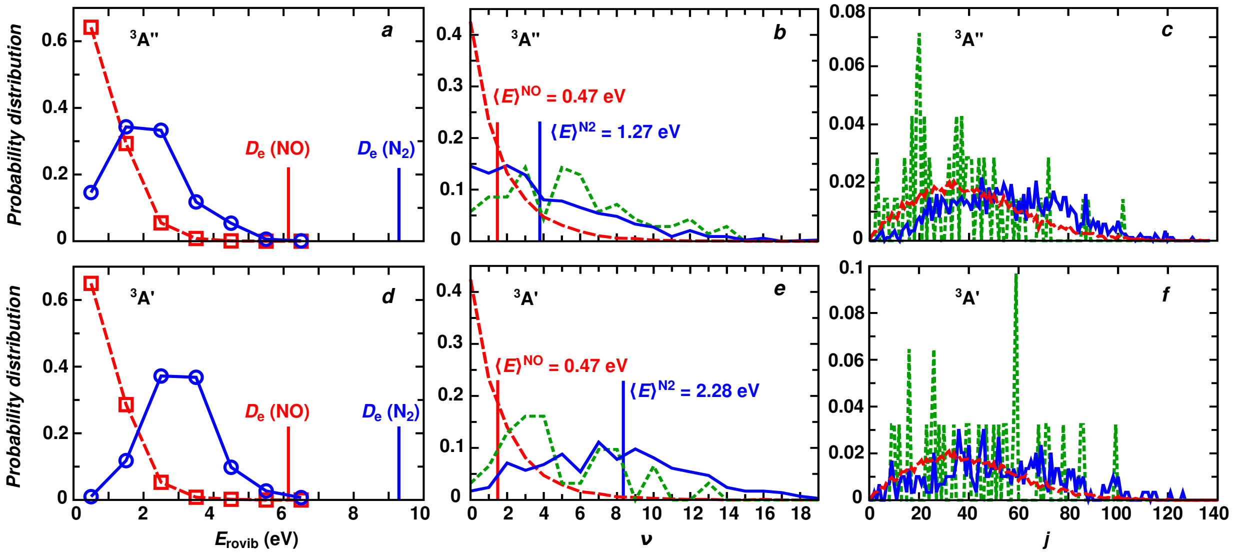

Figure 5: Rovibrational distribution of the products for the NO+N reaction at $T = 5000$ K. Top panels (a-c) are for the simulations on ^{3}A$''$ surface whereas bottom panels (d-f) are for the ^{3}A$'$ PES. Solid and dashed lines correspond to N_2 and NO as the product, respectively. In panels a and d the probabilities are shown in the middle of the interval of rovibrational energies considered. In panels b, c, e, and f, the final NO distributions are separated in two channels: $\mathrm{N}^a\mathrm{O}+\mathrm{N}^b \rightarrow \mathrm{N}^a\mathrm{O}+\mathrm{N}^b$ (red; 9058 events for ^{3}A$''$ and 9672 for ^{3}A$'$), and $\mathrm{N}^a\mathrm{O}+\mathrm{N}^b \rightarrow \mathrm{N}^b\mathrm{O}+\mathrm{N}^a$ (green; 70 events for ^{3}A$''$ and 31 for ^{3}A$'$). For N_2 formation (blue), 872 and 296 events were found for the ^{3}A$''$ and ^{3}A$'$ PESs, respectively. The dissociation energies of NO and N_2 and the averaged vibrational energy of both diatomic molecules (NO and N_2) are also reported.

vibrational and rotational quantum numbers for simulations at $T = 20000$ K. Rovibrational states with energies larger than the dissociation energy of the diatomics were found, contrary to the situation at 5000 K (see Figure 5). At 20000 K, high rotational states are populated and the effective potential, which includes the centrifugal barrier $\left(V^{\mathrm{eff}}(r) = V(r) + \frac{j(j+1)}{2\mu r}\right)$, prevents dissociation. Also, full atomization of the system is possible but only a few trajectories finished in this channel. As this channel is not of particular interest to this work it was not considered further. The probability for the $\mathrm{N}^a\mathrm{O}+\mathrm{N}^b \longrightarrow \mathrm{N}^b\mathrm{O}+\mathrm{N}^a$ channel at 20000 K is 3.1% in the ^{3}A$'$ state and 4.7% for the ^{3}A$''$. This shows the pronounced T-dependence of the atom-exchange channel when compared to the probabilities ($\leq 0.7\%$) at 5000 K. The barrier associated with the $\mathrm{N}^a\mathrm{O}+\mathrm{N}^b \longrightarrow \mathrm{N}^b\mathrm{O}+\mathrm{N}^a$ exchange reaction makes this channel significant only at high temperatures. Figure 6 also shows the NO-vibrational and rotational distributions for the N^{a}O+N^b $\longrightarrow$ N^{a}O+N^b and N^{a}O+N^b $\longrightarrow$ N^{b}O+N^a channels. If no rearrangement occurs during the collision (red trace), the rotational distributions $p(j)$ are close to a Boltzmann distribution. However, the formation of N_2 (blue) and the exchange of nitrogen (green) deviate from an equilibrium thermal distribution but rather displays a dependence on two or more temperatures. Therefore, assuming one temperature for the products is an insufficient approximation although more rigorous sampling of the final states may be required for more quantitative conclusions.

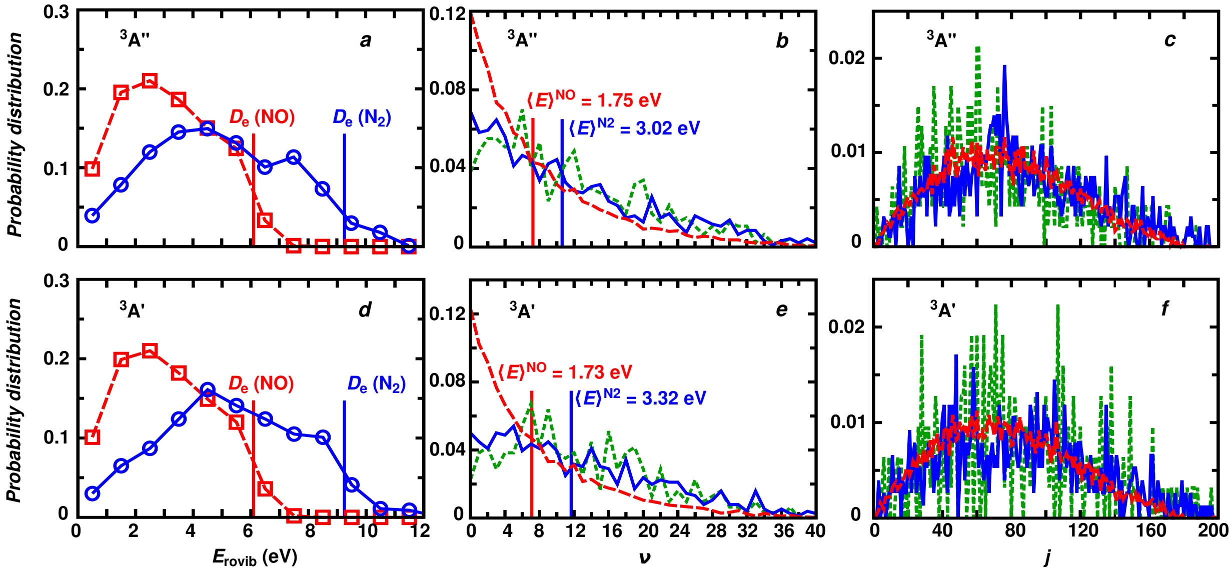

Figure 6: Rovibrational distribution of the products for the NO+N reaction at $T = 20000$ K. Top panels (a-c) are for the ^{3}A$''$ surface whereas bottom panels (d-f) are for the ^{3}A$'$ PES. Solid and dashed lines correspond to N_2 and NO as the product, respectively. In panels a and d the probabilities are shown in the middle of the interval of rovibrational energies considered. In panels b, c, e, and f, the final NO distributions are separated in two channels: N^{a}O+N^b $\rightarrow$ N^{a}O+N^b (red; 8433 events for ^{3}A$''$ and 8714 for ^{3}A$'$), and N^{a}O+N^b $\rightarrow$ N^{b}O+N^a (green; 471 events for ^{3}A$''$ and 313 for ^{3}A$'$). For N_2 formation (blue), 943 and 759 events were found for the ^{3}A$''$ and ^{3}A$'$ PESs, respectively. The dissociation energies of NO and N_2 and the averaged vibrational energy of both diatomic molecules (NO and N_2) are also reported.

Quantum Calculations: An exploratory set of time-independent quantum reactive scattering calculations was performed to validate the QCT calculations using both PESs. The *abc* code[43] was used for studying NO+N collisions at several total energies E_t. This code solves the time-independent Schrödinger equation of a triatomic system using a coupled-channel hyperspherical coordinate method. Quantum scattering conditions are applied exactly and the coupling between initial and final orbital and rotational angular momenta is taken into account for each value of the total angular momentum J.[43] In the present work calculations were carried out for total angular momentum $J = 0$. After initial convergence tests, the maximum value of j included in any channel was 50, and the maximum internal energy was set to 4.0 eV. The value of the maximum hyperradius $\rho_{\max}$, where the asymptotic matching is applied, was 10.6 Å and 400 steps in the log-derivative method were employed. The transition probabilities are determined from the square of the S-matrix elements. A suitable set of QCT trajectories for two values of the collision energies, $E_\mathrm{c} = 0.7$ eV and 1.0 eV, was run from the initial state $\nu = j = J = 0$ (i.e. $b = 0$).[44,45] For the $^3\mathrm{A}'$ state, 6000 QCT trajectories at each E_c were sufficient for convergence, whereas 5000 trajectories were required for convergence using the $^3\mathrm{A}''$ state at a given E_c.

Figure 7 reports the vibrational distribution of the final state of N_2 using quantum and QCT calculations. Overall, the agreement between quantum and classical calculations is good ($^3\mathrm{A}''$, $E_\mathrm{c} = 1.0$ eV) to very good ($^3\mathrm{A}''$, $E_\mathrm{c} = 0.7$ eV and $^3\mathrm{A}'$, $E_\mathrm{t} = 1.0$ eV). In all cases the shape of the distributions are remarkably similar. Only for ($^3\mathrm{A}'$, $E_\mathrm{c} = 0.7$ eV) the QCT simulations slightly overestimate the quantum probability. However, the agreement is still quite good but $p(\nu)$ is very small due to the early barrier in the entrance channel, see Figure 3. Furthermore, the shape of $p(\nu)$ does not change appreciably when increasing the collision energy by 0.3 eV. A similar behaviour was also found for the S+NH reaction.[46] However, the shape of $p(\nu)$ strongly depends of the PES on which the dynamics takes place. Finally, the results from Figure 7 demonstrate the non-equilibrium nature of the final-state distribution $p(\nu)$ at such collision energies for N_2.

Temperature Dependent Rates: Tables 3 and 4 present, respectively, the rate coefficients

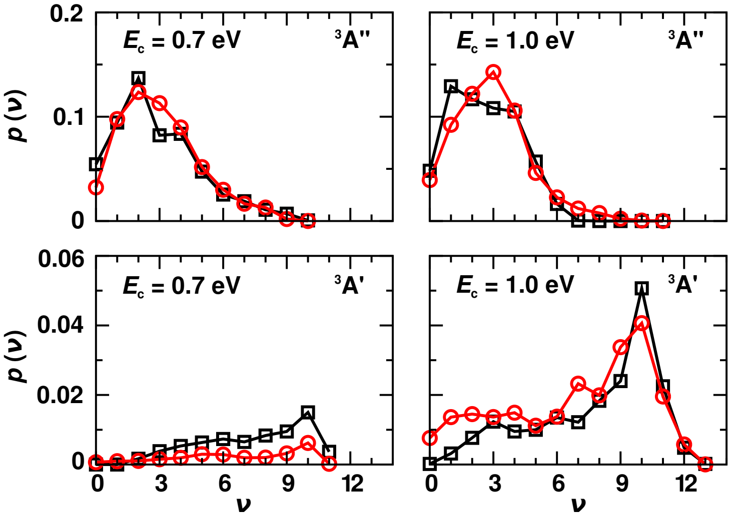

Figure 7: Vibrational energy distribution $p(\nu)$ of N_2 as a product of the $NO(\nu = j = 0)$+N→N_2+O reaction with $J = 0$ using time independent (red lines with circles) and QCT (black line with squares) methods on both PESs, $^3A'$ and $^3A''$.

for the NO+N→N_2+O and $N^aO+N^b \rightarrow N^bO+N^a$ reactions computed using the $^3A''$ and $^3A'$ surfaces. The rate coefficients for N_2 formation increase with temperature for the $^3A'$ state more rapidly than for the $^3A''$ state. This is due to the presence of an early barrier in the $^3A'$ state (see Figure 3). At low temperatures the rates coefficients for the N_2 formation on the $^3A''$ state are at least one order of magnitude higher than those on the $^3A'$ state (see Table 4). However, at higher temperatures (beyond 10000 K), the contribution of both PESs is comparable. The exchange channel is relevant only at high temperatures, due to a barrier at the entry of this channel in both PESs.

Figure 8 reports $k(^3A''+^3A')$ for the NO+N⟶N_2+O reaction (black solid line) together with literature data[13–15,17,18,23,23,24,47–50] in the [100; 5000] K range. In particular, the experimental values recently recommended by the Jet Propulsion Laboratory (JPL)[51] are included (red line), see Figure 8A. Several experiments found that rates increase with temperature while others decrease and similar effects are observed for the calculated rates. Up to $T \approx 1000$ K the $^3A''$ state determines the rate (see Table 3) which is about one order of magnitude smaller compared with most experiments at low temperature (see Figure 8). There are several potential reasons for such disagreement.

First, the PES of the ^{3}A$''$ state could be inaccurate, specifically in the range which controls access of the incoming nitrogen atom, for example at $r = 1.3$ Å in the interval $-1.8 < R\cos\theta < -0.7$ Å, see Figure 4A. It is possible that widening this region of the PES increases the N_2O formation rate which eventually speeds up the overall reaction. However, testing such a proposal would require state-to-state and spectroscopic information from experiments in the entrance channel. In a next step, this could then be used in morphing potential transformations to better define the PES in this region.[42] However, given the good agreement between experiment and simulations at higher temperature, such a localized deficiency of the PES which affects only the rates at low temperature would be surprising.

The discussion above suggests that global deficiencies of the two PESs are unlikely because otherwise the computed high-temperature rates would also be erroneous. It is observed that at 300 K most of the experiments report rates of 2×10^{-11} to 4×10^{-11} which is one order of magnitude larger than the computed rates, see Figure 8. Hence, it is also possible that a mechanism is at play which only operates at lower temperatures ($T < 1000$ K) but is neglected in the present analysis of the problem. Two further scenarios are therefore discussed: 1) there is a crossing between the ^{3}A$'$ and the ^{3}A$''$ state before the barrier in the entrance channel or 2) there is spin conversion early in the entrance channel which allows the system to proceed via a lower-lying state (^{1}A), see Figure 1.

For the first possibility it is noted that the zero point energy in the $v = 0$ state corresponds to a characteristic temperature of 1000 K which is the temperature at which the as yet unspecified process would need to cease contributing to the rate. Analysis of the crossing region between the $^3A''$ and $^3A'$ PESs at the classical turning points of the $v_{\rm NO} = 0$ state indicate that transitions $^3A'' \rightarrow ^3 A'$ are indeed possible. Such a process is not included in the present simulations and can potentially speed up the reaction at low temperature. However, it would also be necessary to close this channel at higher temperatures (i.e. $v > 0$) in order to leave the high-temperature rates unaffected which would imply that the crossing manifold for higher vibrationally excited states change accordingly.

The second possibility involves a spin conversion in the entrance (NO+O→ N_2O) channel from N(^4S) to N(^2D) which would lead to the $^1A'$ manifold, see Figure 1. Such a process has already been investigated for the exit channel (between the O(^3P) and O(^1D) states) by using a Landau-Zener model leading to a rate of $\approx 4 \times 10^{-11}$ cm^3 molecule^{-1} s^{-1}.[11] Hence, with a sufficiently rapid rate for the spin change reaction in the entrance channel the computations could also be reconciled with the experiments at low temperature. At higher temperatures this process would cease to contribute because the crossing velocity becomes too large.

On the other hand, at high temperature ($T > 2000$ K) the experimental rates and those computed here are in good agreement. Furthermore, the theoretical results agree with each other in that the rates increase with temperature above 600 K (see Figure 8B). Previous calculations based on the CASPT2 PES[23] overestimate the recommended rates for $T \geq 1500$ K although at low temperatures they reproduce the experimental values. It is worth to note that these PESs were empirically modified in the entrance channel for reproducing the experimental diatomic dissociation energies and the exoergicity of the reaction, while in the present study the surfaces were not modified.

The electronic degeneracy factor for the N_2 formation channel is of some additional concern. Because the N_2O intermediate may or may not be stabilized (depending on the details of the collision) an electronic degeneracy factor of $g'_e = q_{\rm product}/q_{\rm reactant}$ with $q_{\rm product} = q_{\rm O(^3P)} q_{\rm N_2(^1\Sigma)}$ where $q_{\rm O(^3P)} = 5 + 3\exp(-227.7/T) + \exp(-326.6/T)$,[23] and $q_{\rm N_2(^1\Sigma)} = 1$, and $q_{\rm reactant} =$

$q_{NO(^2\Pi)}q_{N(^4S)}$ would be equally possible. Using this expression instead of Eq. 14, the resulting rate coefficients are also indicated in Figure 8 (dashed black line).

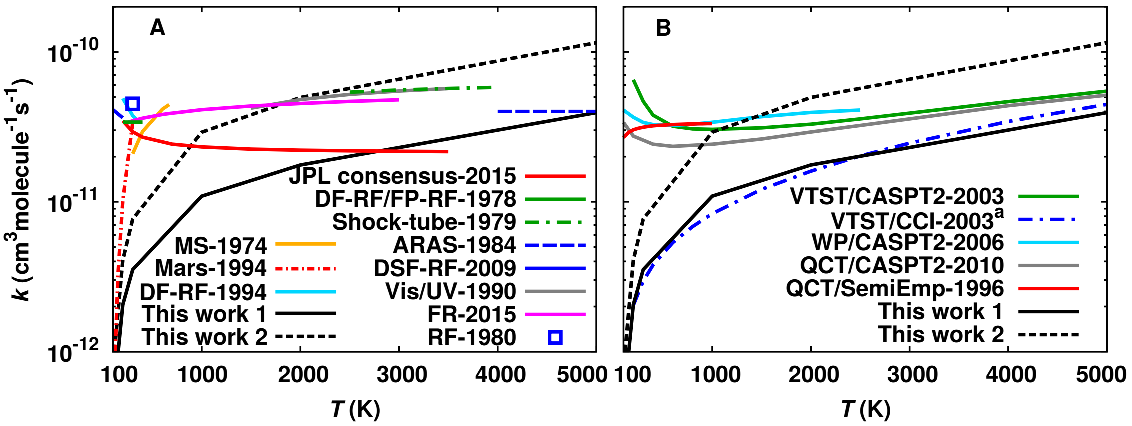

Figure 8: Rate coefficients for N_2 formation at temperatures 100 $K \leq T \leq$ 5000 K. The black solid lines (This work 1) are the rates using the g_e defined in equation 14, while the black dashed lines (This work 2) correspond to an alternative g_e (see the text). In panel A the results of the present work are compared with experiments. A comparison with published theoretical is provided in in panel B. The method of determination of the rates and the years of publication are pointed in each case and the Shock-tube-1979 and ARAS-1984 were were derived from measuring the reverse reaction and using the K^{eq} derived from the CEA database. Data taken from Mars-1994,[15] DF-RF-1994,[14] MS-1975,[18]JPL consensus-2015,[51] DF-RF/FP-RF-1978,[17] Shock-tube-1979,[52] rev-ARAS-1984,[53] DSF-RF-2009,[13] Vis/UV-1990,[47]FR-2015,[54] RF-1980,[55] VTST/CASPT2-2003,[23] VTST/CCI-2003 dynamic calculations reported in Ref[23] using the PESs from,[21,56] WP/CASPT2-2006,[24] QCT/CASPT2-2010,[49] and QCT/SemiEmp-1996.[50]

Table 3: Rate coefficients (cm^{3}molecules^{-1}s^{-1}) of the NO($^2\Pi$)+N(^4S)→N_2($^1\Sigma$)+O(^3P) reaction at several temperatures, using the $g_e(T)$ defined in Equation 14. The standard deviation (68% statistical uncertainty) is also reported for the total rates.

T (K)	$k(^3A')$	$k(^3A'')$	$k(^3A'')+k(^3A')$
100	—	4.44×10^{-13}	$(4.44 \pm 0.64) \times 10^{-13}$
200	—	2.06×10^{-12}	$(2.06 \pm 0.16) \times 10^{-12}$
300	—	3.53×10^{-12}	$(3.53 \pm 0.23) \times 10^{-12}$
1000	9.16×10^{-14}	1.08×10^{-11}	$(1.09 \pm 0.05) \times 10^{-11}$
2000	1.24×10^{-12}	1.64×10^{-11}	$(1.76 \pm 0.07) \times 10^{-11}$
5000	9.72×10^{-12}	2.96×10^{-11}	$(3.93 \pm 0.13) \times 10^{-11}$
10000	3.13×10^{-11}	4.88×10^{-11}	$(8.01 \pm 0.23) \times 10^{-11}$
15000	4.36×10^{-11}	5.75×10^{-11}	$(1.01 \pm 0.03) \times 10^{-10}$
20000	5.46×10^{-11}	6.81×10^{-11}	$(1.23 \pm 0.03) \times 10^{-10}$

Table 4: Rate coefficients ($cm^3 molecules^{-1} s^{-1}$) of the $N^aO+N^b \rightarrow N^aO+N^b$ reaction at several temperatures, using the $g_e(T)$ defined in Equation 14. The standard deviation (68% statistical uncertainty) is also reported for the total rates.

T (K)	$k(^3A')$	$k(^3A'')$	$k(^3A'')+k(^3A')$
5000	7.22×10^{-13}	1.41×10^{-12}	$(2.13 \pm 0.23) \times 10^{-12}$
10000	7.04×10^{-12}	1.14×10^{-11}	$(1.85 \pm 0.10) \times 10^{-11}$
15000	1.68×10^{-11}	2.19×10^{-11}	$(3.87 \pm 0.17) \times 10^{-11}$
20000	2.20×10^{-11}	2.75×10^{-11}	$(4.94 \pm 0.21) \times 10^{-11}$

The rate coefficients at temperatures relevant for the hypersonic flight regime are shown in Figure 9. The predicted rates increase with increasing T. Also, the exchange channel becomes important at sufficiently high temperatures ($T \geq 10000$ K). This is essential information for meaningful modelling of the reaction involved in the hypersonic flight regime as this generates NO in high vibrationally excited states. For modelling re-entry conditions the use of an empirical expression that describes the rate coefficients is often quite useful. Fitting an Arrhenius expression between 5000 and 20000 K yields for the exchange channel ($k(T)$ from Table 4)

$$k^{\text{exch}}(T) = 1.475 \times 10^{-10} \exp(-20907.67/T) \tag{16}$$

and for N_2 formation ($k(T)$ from Table 3)

$$k(T) = 1.712 \times 10^{-10} \exp(-7423.430/T) \tag{17}$$

Furthermore, a more general expression for the $NO+N \rightarrow N_2+O$ reaction valid over the temperature range from (1000 K to 20000 K) using a modified Arrhenius expression is

$$k_{\text{mod}}(T) = 2.421 \times 10^{-14} T^{0.867} \exp(-102.447/T) \tag{18}$$

and for the exchange reaction this expression is

$$k_{\mathrm{mod}}^{\mathrm{exch}}(T) = 2.192 \times 10^{-5} T^{-1.146} \exp(-35054.530/T) \tag{19}$$

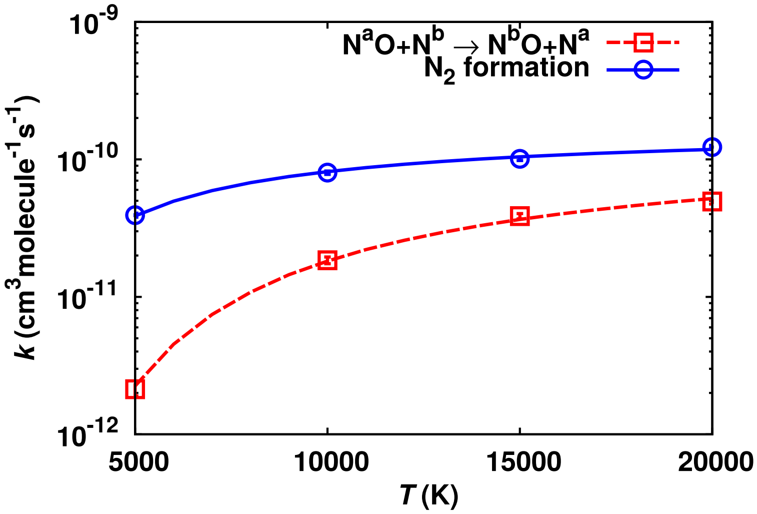

Figure 9: Rate coefficients for the NO+N reaction for the atom exchange (squares) and N_2 formation channels (circles) from 5000 K to 20000 K. The points are the computed rates and the lines correspond to the expressions in Eqs. 16 and 17 and $g_e(T)$ from Eq. 14.

4 Summary

The two lowest triplet PESs of N_2O correlating with NO($X^2\Pi$)+N(^4S) and N_2($X^1\Sigma$)+O(^3P) from *ab initio* calculations were determined at the MRCI+Q level of theory. The energies in each asymptotic channel were represented as a reproducing kernel which exactly reproduces the MRCI+Q energies. Quasiclassical trajectory calculations using these new PESs were performed for temperatures up to $T = 20000$ K and the rate coefficients were determined. The calculations suggest that up to 5000 K N_2 formation occurs entirely on the ^{3}A$''$ PES whereas reactions involving the ^{3}A$'$ state start to contribute above that. Below 1000 K the experimental results are quite heterogeneous but typically one order of magnitude faster than the computed rates. Conversely, at temperatures above 3000 K the agreement is encouraging. At sufficiently high temperatures ($T \geq 10000$K) the final state distributions show non-Boltzmann behaviour. Hence, although reaction rates can be computed, they do not necessarily correspond to a thermal ensemble. The high-temperature rates determined in the present work will be a useful input for modeling atmospheric re-entry. However, further work based on non-equilibrium initial conditions will also be relevant for a full account of the problem.

At low temperatures, the computations yield low rate coefficients consistent with VTST/CCI calculations and the rate derived from models of the measurements in Mars atmosphere but disagree with other theoretical and experimental data whereas for temperatures relevant to the present work ($T \geq 5000$ K), agreement with available data is quite favourable. Above 1000 K the results of the present study are in good agreement with the experimentally recommended values. At temperatures below 5000 K the N_2 formation and the nitrogen exchange reactions takes place mainly on the $^3A''$ surface. The average vibrational energies for N_2 formation on the two PESs differs by > 1 eV which will be a useful benchmark for future energy-resolved experiments to confirm and support the present calculations. At higher temperatures the average N_2 vibrational energies differ far less for the two PESs and the contribution of both electronic states to the reaction rate should be considered.

Acknowledgments

Part of this work was supported by the United State Department of the Air Force which is gratefully acknowledged (to ODA). Support by the Swiss National Science Foundation through grants 200021-117810, the NCCR MUST (to MM), and the University of Basel is also acknowledged.

References

(1) Armenise, I.; Esposito, F. *Chem. Phys.* **2015**, *446*, 30–46.

(2) Li, J.; Varandas, A. J. *J. Phys. Chem. A* **2012**, *116*, 4646–4656.

(3) Li, J.; Caridade, P. J.; Varandas, A. J. *J. Phys. Chem. A* **2014**, *118*, 1277–1286.

(4) González, M.; Valero, R.; Sayós, R. *J. Chem. Phys.* **2000**, *113*, 10983–10998.

(5) Black, G.; Slanger, T.; St John, G.; Young, R. *J. Chem. Phys.* **1969**, *51*, 116–121.

(6) Lin, C.-L.; Kaufman, F. *J. Chem. Phys.* **1971**, *55*, 3760–3770.

(7) Fell, C.; Steinfeld, J.; Miller, S. *J. Chem. Phys.* **1990**, *92*, 4768–4777.

(8) Husain, D.; Kirsch, L.; Wiesenfeld, J. *Faraday Discuss. Chem. Soc.* **1972**, *53*, 201–210.

(9) Husain, D.; Mitra, S. K.; Young, A. N. *J. Chem. Soc., Faraday Trans. 2* **1974**, *70*, 1721–1731.

(10) Sugawara, K.; Ishikawa, Y.; Sato, S. *Bull. Chem. Soc. Jpn.* **1980**, *53*, 3159–3164.

(11) Tachikawa, H.; Hamabayashi, T.; Yoshida, H. *J. Phys. Chem.* **1995**, *99*, 16630–16635.

(12) Strekowski, R.; Nicovich, J.; Wine, P. *Phys. Chem. Chem. Phys.* **2004**, *6*, 2145–2151.

(13) Bergeat, A.; Hickson, K. M.; Daugey, N.; Caubet, P.; Costes, M. *Phys. Chem. Chem. Phys.* **2009**, *11*, 8149–8155.

(14) Wennberg, P. O.; Anderson, J. G.; Weisenstein, D. K. *J. Geophys. Res. Atmos.* **1994**, *99*, 18839–18846.

(15) Fox, J. L. *J Geophys Res Space Phys* **1994**, *99*, 6273–6276.

(16) Jeoung, S. C.; Choo, K. Y.; Benson, S. W. *J. Phys. Chem.* **1991**, *95*, 7282–7290.

(17) Lee, J.; Michael, J.; Payne, W.; Stief, L. *J. Chem. Phys.* **1978**, *69*, 3069–3076.

(18) Clyne, M. A.; McDermid, I. S. *J. Chem. Soc., Faraday Trans. 1* **1975**, *71*, 2189–2202.

(19) Kistiakowsky, G.; Volpi, G. *J. Chem. Phys.* **1958**, *28*, 665–668.

(20) Hopper, D. G. *J. Chem. Phys.* **1984**, *80*, 4290–4316.

(21) Bose, D.; Candler, G. V. *J. Chem. Phys.* **1996**, *104*, 2825–2833.

(22) Bose, D.; Candler, G. V. *J. Thermophys Heat Transfer* **1996**, *10*, 148–154.

(23) Gamallo, P.; González, M.; Sayós, R. *J. Chem. Phys.* **2003**, *119*, 2545–2556.

(24) Gamallo, P.; Sayós, R.; González, M.; Petrongolo, C.; Defazio, P. *J. Chem. Phys.* **2006**, *124*, 174303.

(25) Lin, W.; Meana-Pañeda, R.; Varga, Z.; Truhlar, D. G. *J. Chem. Phys.* **2016**, *144*, 234314.

(26) Lin, W.; Varga, Z.; Song, G.; Paukku, Y.; Truhlar, D. G. *J. Chem. Phys.* **2016**, *144*, 024309.

(27) Nagy, T.; Yosa Reyes, J.; Meuwly, M. *J. Chem. Theo. Comp.* **2014**, *10*, 1366–1375.

(28) Langhoff, S. R.; Davidson, E. R. *Int. J. Quant. Chem.* **1974**, *8*, 61–72.

(29) Dunning, T. H. *J. Chem. Phys.* **1989**, *90*, 1007.

(30) Werner, H.-J.; Knowles, P. J.; Knizia, G.; Manby, F. R.; Schütz, M. *Wiley Interdisciplinary Reviews: Computational Molecular Science* **2012**, *2*, 242–253.

(31) Ho, T.-S.; Rabitz, H. *J. Phys. Chem.* **1996**, *104*, 2584.

(32) Unke, O. T.; Castro-Palacio, J. C.; Bemish, R. J.; Meuwly, M. *J. Chem. Phys.* **2016**, *144*, 224307.

(33) Castro-Palacio, J. C.; Nagy, T.; Bemish, R. J.; Meuwly, M. *J. Chem. Phys.* **2014**, *141*, 164319.

(34) Castro-Palacio, J. C.; Bemish, R. J.; Meuwly, M. *J. Chem. Phys.* **2015**, *142*, 091104.

(35) Codes for the NO+N potential energy surfaces. `https://github.com/MeuwlyGroup/N2O-triplets`, Online; accessed November 2016.

(36) Huber, K. P.; Herzberg, G. *Molecular Spectra and Molecular Structure. IV. Constants of Diatomic Molecules*; Van Nostrand Reinhold: New York, 1979.

(37) Verlet, L. *Phys. Rev.* **1967**, *159*, 98.

(38) Liboff, R. L. *Introductory quantum mechanics*; Addison-Wesley, 2003.

(39) Porter, R.; Raff, L.; Miller, W. *J. Chem. Phys.* **1975**, *63*, 2214–2218.

(40) Daan, F.; Berend, S. *Understanding molecular simulation: From algorithms to applications*; Academic Press: San Diego, California, 2002.

(41) Okabe, H. *Photochemistry of small molecules*; Wiley, New York, 1978.

(42) Meuwly, M.; Hutson, J. M. *J. Chem. Phys.* **1999**, *110*, 8338–8347.

(43) Skouteris, D.; Castillo, J.; Manolopoulos, D. *Comput. Phys. Commun.* **2000**, *133*, 128–135.

(44) Landau, L. D.; Lifschitz, E. M. *Mechanik*; Akademie-Verlag: Berlin, 1990.

(45) Banares, L.; Aoiz, F.; Honvault, P.; Bussery-Honvault, B.; Launay, J. *J. Chem. Phys.* **2003**, *118*, 565–568.

(46) Sato, K.; Takayanagi, T. *Chem. Phys.* **2014**, *439*, 63–70.

(47) Davidson, D.; Hanson, R. *Int. J. Chem. Kinet.* **1990**, *22*, 843–861.

(48) Siskind, D. E.; Rusch, D. W. *J Geophys Res Space Phys* **1992**, *97*, 3209–3217.

(49) Gamallo, P.; Martínez, R.; Sayós, R.; González, M. *J. Chem. Phys.* **2010**, *132*, 144304.

(50) Duff, J.; Sharma, R. *Geophys. Res. Lett.* **1996**, *23*, 2777–2780.

(51) Burkholder, J.; Abbatt, J.; Huie, R.; Kolb, C.; Orkin, V.; Wine, P.; Sander, S.; Barker, J.; Kurylo, M.; Wilmouth, D. *Chemical Kinetics and Photochemical Data for Use in Atmospheric Studies: Evaluation Number 18*; 2015.

(52) Monat, J.; Hanson, R.; Kruger, C. Shock tube determination of the rate coefficient for the reaction N 2+ O NO+ N. Symposium (International) on Combustion. 1979; pp 543–552.

(53) Thielen, K.; Roth, P. Resonance absorption measurements of N and O atoms in high temperature NO dissociation and formation kinetics. Symposium (International) on Combustion. 1985; pp 685–693.

(54) Abian, M.; Alzueta, M. U.; Glarborg, P. *Int. J. Chem. Kinet.* **2015**, *47*, 518–532.

(55) Husain, D.; Slater, N. K. *J. Chem. Soc., Faraday Trans. 2* **1980**, *76*, 606–619.

(56) Gilibert, M.; Aguilar, A.; Gonzalez, M.; Mota, F.; Sayós, R. *J. Chem. Phys.* **1992**, *97*, 5542–5553.